

# EXTENDED-TIME PROCESS CONSISTENCY AND PROCESS-PROPERTY RELATIONSHIPS FOR FLEXIBLE ADDITIVE-PRINTED ELECTRONICS

Pradeep Lall, Nakul Kothari, Kartik Goyal  
Auburn University  
NSF-CAVE3 Electronics Research Center  
Department of Mechanical Engineering  
AL, USA  
lall@auburn.edu

Ben Leever  
US Air Force Research Labs  
Wright-Patterson AFB  
OH, USA

Scott Miller  
NextFlex Manufacturing Institute  
CA, USA

## ABSTRACT

Traditionally, a combination of imaging and plating based subtractive processes have been used for fabrication of printed circuit assemblies to form the needed circuitry on rigid and flexible laminates. In addition to circuits, additive electronics is finding applications for fabrication of sensors for wearable applications and asset situational awareness. Aerosol-Jet printing has shown the capability for printing lines and spaces below 10  $\mu\text{m}$  in width with a wide variety of materials, including nanoparticle inks, conductive polymers, insulators, adhesives, and even biological matter. The adoption of additive manufacturing for high-volume commercial fabrication requires an understanding of the print consistency, electrical and mechanical properties. In this study, the effect of process parameters on the resultant line-consistency, mechanical and electrical properties has been studied for single-layer and multi-layer substrates. Print process parameters studied include the sheath rate, mass flow rate, nozzle size, substrate temperature and chiller temperature. Properties include resistance and shear load to failure of the printed electrical line as a function of varying sintering time and varying sintering temperature. Printed samples have been exposed to different sintering times and temperatures. The resistance and shear load to failure of the printed lines has been measured. The underlying physics of the resultant trend was then investigated using elemental analysis and SEM. The effect of line-consistency drift over prolonged runtimes has been measured for up to 10-hours of runtime. Printing process efficiency has been gauged a function of process capability index (Cpk) and process capability ratio (Cp). Printed samples were studied offline using optical Profilometry to analyze the consistency within the line width, line height, line resistance and shear load to study the variance in the electrical and mechanical properties over time.

Key words: Additive Printed Electronics, Aerosol Jet, Flexible Electronics.

## INTRODUCTION

Technologies for producing printed electronics have gained much popularity because of their low ramp-up time, simplified fabrication procedures, ability to fabricate varied complex functional devices and relatively high print resolutions in comparison to incumbent trace metallization processes. Advantages of printed electronics have driven growth of application area in a number of market segments. A recent reports point to the growth of printed electronics with applications, which span, displays, conductive inks, printed flexible sensors, lighting, and batteries [IDTechEx 2018]. The growth rate of flexible printed electronics has been high with reported growth in the neighborhood of 29-percent as recently as 2012 [BCC 2012]. The strong growth rate of flexible printed electronics is expected to continue with predicted growth rate of 14.9-percent between 2018-2023 [Markets 2018]. In recent times, the main market for printed electronics is found to be in the low-end devices with low fabrication costs in addition to customized electronics [Lupo 2013]. Manufacturing of application-specific electronics using existing printing infrastructure like flexography, gravure printing, offset lithography printing or screen-printing is prohibitively expensive because of the wastage of raw material and large-area print format.

The use of Aerosol Jet Printing allows for the use of multiple print heads, each capable of carrying different ink with different viscosities. The print tool-paths are driven by computer-aided design models. The process uses pressurized inert gas to focus a beam of aerosol (nano-particles) onto a substrate. The elimination of the need for masks and tooling

for printing allows quick ramp-up without extensive setup costs associated with traditional existing techniques. The process can handle inks with varying viscosities ranging from 1 to 1000 cP, using either Ultrasonic atomization or Pneumatic atomization of the ink. In addition, the use of different printing standoff distance and sample orientation allows for printing on non-planar or curved surfaces. Previous researchers have published upon use of AJP for printing 3D conformal electronics with micron-scale features, micro-vias [Paulsen 2012, Krzeminski 2017]. The feasibility of using aerosol-jet printing has been demonstrated for a number of applications including passive microwave circuitry [Cai 2014] and quasi-optical terahertz filters [Oakley 2017]. A number of prior studies focus on the feasibility of the use of aerosol-jet printing on a number of substrates. Aerosol-jet printing has been studied for compatibility with first-level interconnects including wire bonding [Stoukatch 2012], for printing sensors for Internet of Things applications [Navratil 2018], printing on silicon solar cells [King 2009], making electrical contacts in SOI MEMS [Khorramdel 2018]. A number of material and process parameters may impact print process output including parameters of the atomization process, ink, substrate, and print-environment (Figure 1).

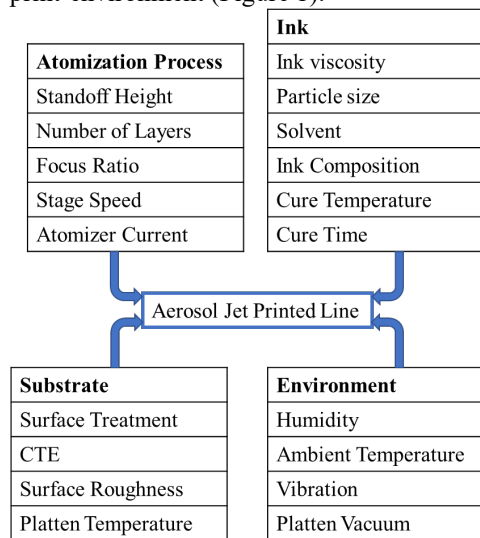


**Figure 1:** Parameters affecting AJP line properties

In this paper, the correlation of the mechanical properties of aerosol jet printed lines with process parameters has been studied. The reliability of the aerosol-jet printed traces has been correlated to the mechanical properties and electrical properties of the printed lines. The elastic modulus, the shear modulus or shear load to failure, resistivity of the printed line have been used for selection of suitable ink type, process parameters and sintering times and temperatures. Process parameters studied include sheath flow rate, ink flow rate, stage speed, standoff height, chiller temperature, platen temperature (Figure 1). Better understanding of the effect of each process parameter in the printed lines will allow users to select appropriate process parameters for design functional performance. In addition, the development of process-property relationships will provide visibility into the critical

parameters, which require added level of attention for process-control. In addition, the process parameter drift over a long production run may be important for a high-volume production environment. The effect on the print process may be in the form of line consistency, and resistance – both of which have been quantified in this study. A procedure for finding process parameters that minimize the resistivity of printed lines has been developed. Effect of sintering time, and sintering temperature on the mechanical and electrical properties of the printed lines has been quantified. Scanning electron micrographs have been used to understand the electrical and mechanical behavior of printed traces. The study results have been used to develop processes for multi-layer substrates. A statistical approach is presented for prediction of physical attributes of multilayer circuits micro-via diameter for the dielectric and line widths and resistance for the metal conductive line before starting the print process. The model can also be used to pre-adjust the CAD file dimensions to obtain the desired characteristics. Next, process parameters are developed for a multi-layer print consisting of metal Nano-particle ink as a conductive path and an electronic adhesive as a dielectric to provide the insulation between two conductive paths. Finally, printing process efficiency is gauged as a function of process capability index ( $C_{pk}$ ) and process capability ratio ( $C_p$ ).

### ADDITIVE PRINTING METHODS

The Aerosol Jet Printer uses a combination of a pneumatic atomizer, an ultrasonic atomizer, a deposition head, a process control module (PCM) and a 3-axis linear and rotational motion driver for printing lines. The ultrasonic atomizer (Figure 2) is used for inks with low viscosity and small solid particle sizes (< 100 nm). The pneumatic atomizer (Figure 3) is required for inks with high viscosity (particle size up to 500 nm).

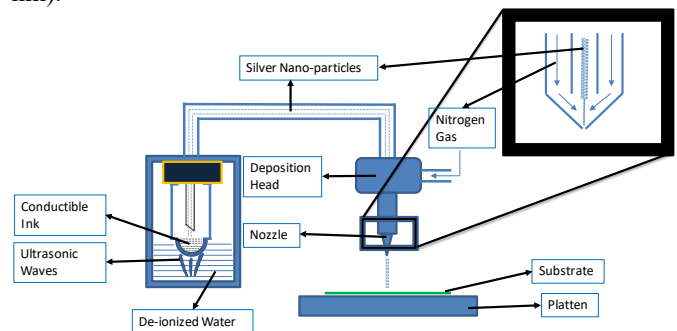


**Figure 2:** Principle of Ultrasonic Atomization

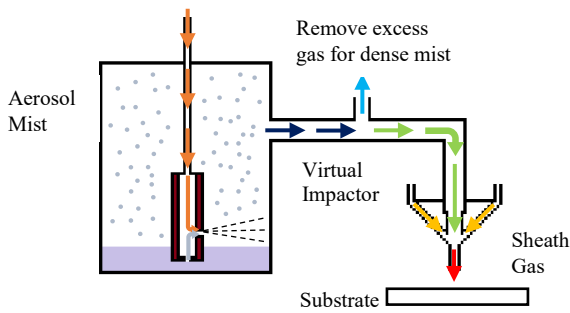


**Figure 3:** Principle of Pneumatic Atomization

Once the ink has been aerosolized in the atomizer, it is carried by the carrier gas, and aerodynamically focused in the print head into a concentrated beam and then projected onto the substrate. The deposited inks are sintered or cured based on properties of the material type and substrate. Sintering profiles are controlled through specification of the sintering temperature and sintering time. The width of the aerosol beam and thus the line width of the applied layers may be influenced by a number of parameters including among them the ratio of sheath gas to aerosol stream in the deposition head. This ratio is called the Focus Ratio. Increasing amounts of sheath gas results in a compression of the aerosol stream. Furthermore, line width increases with greater nozzle distance from the substrate. Gas flows and aerosol formation can be controlled via the process control module of the Aerosol Jet system. The print process can be separated into the following 4-stages [Secor 2018] including (1) Aerosol generation (2) Aerosol transport (3) Aerosol jet collimation (4) Impaction on substrate.

Optomec AJ-300 employs two-types of aerosol generators, an ultrasonic atomizer and a pneumatic atomizer. Depending on the viscosity of the ink, a suitable atomizer may be selected. Generally, an ink with higher viscosity (>30cP) is used with pneumatic atomizer and an ink with viscosity lower than 30cP may be used with ultrasonic atomizer. Ultrasonic atomizer has an ultrasonic bath underneath the vial containing ink. A piezoelectric actuator outputs ultrasonic waves, which travel upwards through deionized water as the medium, and sets up a capillary wave on the ink surface leading to the formation of ink droplets with a defined size distribution [Lang 1962; Peskin 1963]. The size of the droplet thus formed is dependent on the capillary wavelength, frequency, ink density and the ink surface tension [Rodes 1990]. The ink droplets are suspended in a solvent and cosolvent, which forms the ink. In order to prevent drying of the aerosol droplets, inks commonly have approximately 10-percent of low volatility cosolvent [Ha 2013]. Upon atomization, when the ink droplets meet a dry gas, the solvent evaporates [Ravindran 1982; Widmann 1997]. The closed enclosure that carries the atomized becomes saturated with solvent vapor in matter of seconds once the process has started.

Once the aerosol droplets are formed, they are carried to the deposition head in a plastic tube. It has been reported that, on an average it takes 10s for droplets generated to travel through the tube and reach the deposition head. During the process of droplet transport, some droplets collide with the inner walls of the tube and never reach the deposition head. Collision of the droplets with the inner walls of the tube is a source of losses attributed to the two mechanisms of gravitational settling and diffusion. Among the droplets being generated, larger sized droplets are susceptible to gravitational settling and smaller droplets are susceptible to diffusion. These mechanisms largely govern the output of the atomized ink on the substrate. When the droplets come out of the deposition nozzle, the aerosol droplets travel towards the substrate carried by the carrier gas. Smaller diameter droplets in the flow stream owing to their smaller mass may be carried away from the deposition axis by the sheath gas coming out of the nozzles. Increase in the sheath-gas flow rate increases the jet velocity minimizing spreading of the droplet stream. The distribution of the droplet size in the aerosol spray results in a line, which has a dense core region surrounded by a diffuse overspray. The flow rate, sheath gas flow rate, focus ratio, nozzle diameter, and ink droplet size determine the profile of the printed lines. In general, overspray is associated with larger diameter nozzles, low total flow rate, and a low sheath-to-flow rate ratio or low focus ratio. Further, a more stable size distribution of the droplet would result in printed lines with relatively lesser overspray and well-defined line edges. Well defines edges also result in more uniform cross section, resulting in lesser resistivity.

**CONDUCTIVE INKS AND DIELECTRICS**

The inks used in this study were silver nano-particle based inks. A detailed formulation of the ink-A is given in the Table 1 and for ink-B is given in Table 2. The properties for the interlayer dielectric ink-C are shown in Table 3

**Table 1:** Conductive Ink-A Formulation

Properties	Value
Viscosity (cP)	15cP
Particle Size (nm)	70nm
Silver Concentration (wt. %)	50 ± 2 percent
Sintering Profile	200°C; 1hr
Color	Brown
Storage Temp (°C)	20-25°C
Solvent	Ethylene glycol

**Table 2:** Conductive Ink-B Formulation

Properties	Value
Viscosity (cP)	1 – 30 cP
Particle Size (nm)	8 – 15 nm
Silver Concentration (wt. %)	40 – 60 percent
Sintering Temperature (°C)	120 – 300°C
Solvent	Xylene, Terpeneol and Hydrocarbons (Proprietary)

**Table 3: ILD Ink-C Formulation**

Property	Value
Viscosity at 25° C (cP)	300 cps
Elongation at Failure (%)	30 percent
Modulus of Elasticity (psi)	160,000
Tensile Strength (psi)	3,500
Hardness - Shore D	85
Total Mass Loss (TML)	3.14 percent
Collected Volatile Condensable Material (CVCM)	0.41 percent
Dielectric Constant (1 MHz)	4.04
Dissipation Factor (1 MHz)	0.045
Volume Resistivity (ohm-cm)	$1.0 \times 10^{15}$
Surface Resistivity (M $\Omega$ )	$10 \times 10^9$
Dielectric Strength (volts/mil)	980
Arc Resistance (sec)	95

Given the low viscosity of the ink-A and ink-B, the ultrasonic atomizer was used for aerosol jet process. The ink has a nominal particle size of 70nm. Recommended sintering temperature of the ink-A is 200°C for 60 minutes in a conventional thermal chamber or oven. The ink has a density of 1.8 g/cm<sup>3</sup> and a shelf life of 6 months. The recommended curing temperature for conductive ink-B is in the range of 120-300°C. The ILD Ink-C is UV curable.

#### IDENTIFICATION OF PROCESS PARAMETERS

Conductive Ink-A data is presented in this section. Aerosol-Jet printing process parameters have been selected through the design of an experimental matrix and measurement of performance of the printed lines. Parameters controlled include, sheath gas flow rate, ink flow rate, focus ratio, stage speed, standoff height, nozzle diameter, chiller temperature, platen temperature are just the most important process parameters. In addition to the print parameters, a number of post-print parameters affect the performance of the printed line including the sintering profile quantified by the sintering time and sintering temperature.

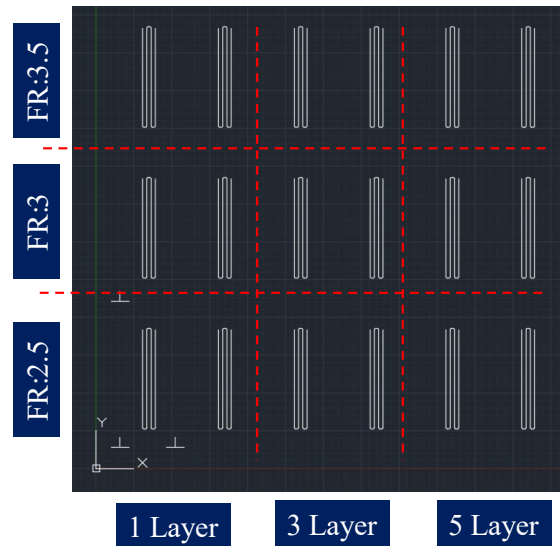


**Figure 4:** Print pattern and matrix for finding process parameters that minimize resistivity

Once the lines are printed, and before the process of sintering, the printed lines are just an agglomeration of nanoparticles or nanoflakes. Exposure to heat through thermal sintering, photonic sintering or laser sintering causes the silver nanoparticles to melt and form more coherent traces through surface melting and compaction of the particles. In addition to resistivity, sintering affects the mechanical properties like shear strength and elastic modulus of the line. In this study, the search for desirable process parameters has been guided by the configuration that provided the lowest resistivity. The effect of the sintering profiles has been quantified on the electrical properties including resistivity and mechanical properties, including the shear strength and the elastic modulus. Three different FR and three different number of passes or layers were printed and sintered at the stipulated print profile of 200°C for 60 minutes. First, lines with different ink flow rate and sheath gas flow rates were printed at a standoff height of 3mm from the substrate, chiller temperature of 20°C and stage speed ranging from 0.3 to 1mm per sec. The lines obtained were examined under an optical microscope to check for continuity. It was found that, an ink flow rate of 20sccm and sheath-gas flow rate ranging from 50sccm and above at a speed of 0.5mm per sec lead to continuous lines.

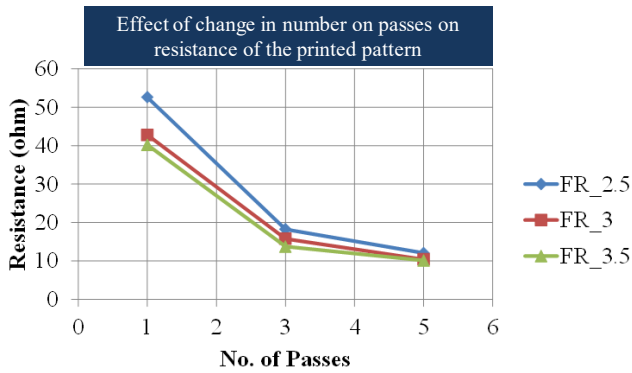


**Figure 5:** Effect of change in number on passes on resistance of the printed pattern for Conductive Ink-A

Schematic of the pattern to be printed was designed in a CAD modeling software and imported as a program file (g codes and m codes). The print pattern with varying FR and number of layers is shown in Figure 4. This test matrix of pattern was printed on to the large 2 inches by 3-inch substrate. The cleaning process of the substrate was set to be constant and not varied in the experimental matrix. Each substrate was cleaned with Acetone and Iso-propyl alcohol and blow dried with compressed air prior to printing. The AJ300 machine doors were kept closed at all times during the printing process to prevent any disruption in the aerosol jet during the printing process from airflow in the room.

**Table 4:** Finalized process parameters for Ink-A

Process Parameter	Value
Ink mass flow rate	20 sccm
Sheath gas flow rate	75 sccm
Stage Speed	0.5mm/s
Stand-off height	3mm
Nozzle diameter	150microns
Number of passes	5

The printed lines were probed on a resistance spectroscopy equipment to measure the resistance. The focus ratio was adjusted by only changing the sheath-gas flow rate, without changing the ink flow rate. The figure below is a graph of resistance vs number of layers. The resistance of the printed lines decreased with the increase in the number of print-passes. It was observed that improvement in resistance from 1-pass to 3-passes, for a FR of 3.5 was ~65% and the improvement from 3 passes and 5 passes was ~28%. The average resistance value found at 5-passes for all the FRs was found to be in the range of 10Ω to 14Ω, indicating that the gains in resistance value diminish beyond 5-passes. Thus, 5-passes were decided upon as the final number of layers. In addition, focus ratio of 3.5 was also observed to give the least resistance value in the graph as expected. The process parameters finalized that lead to least resistance are stated in Table 4. These parameters were used throughout the remainder of the study.

## PROCESS-PERFORMANCE TEST MATRIX

Once the process parameters were finalized, a detailed study was conducted to understand the correlation of mechanical and electrical properties of the printed lines with variation in sintering times and temperatures. The process parameters of the additively printed traces have been correlated to the mechanical and electrical properties of these micro-scale printed lines. The measured data fills a void in literature for additively printed interconnects. Properties including elastic modulus, shear load to failure, resistivity are available for conventional electrical traces that are manufactured through subtractive printing process. The conventional traces are typically treated as homogenous linear isotropic materials – an assumption that breaks down for additively printed lines. Additively printed lines are instead a collection of spheres, or flakes depending on the ink formulation.

**Table 5:** Sintering temperatures for Conductive Ink-A

Sintering Temperature	Sintering Time	Resistance	Shear Load to failure	Elastic modulus
200°C	60 min	X	X	X
240°C	60 min	X	X	X
280°C	60 min	X	X	X
300°C	60 min	X	X	X

**Table 6:** Sintering times for Conductive Ink-A

Sintering Temperature	Sintering Time	Resistance	Shear Load to failure
200°C	60 min	X	X
200°C	105 min	X	X
200°C	150 min	X	X
200°C	180 min	X	X

Furthermore, when nano-sized particles are additively printed to form electrical traces that are much longer in length with respect to its width, with multiple print passes made, the resultant structure is anisotropic in nature. The material properties are dependent on the geometry of the resultant structure and the geometry is dependent on process variations. A test matrix has been developed to study the effect of varying sintering time and temperature on resistivity and mechanical properties of the printed line. Table 5 and Table 6 show the test matrices for sintering temperature and sintering time respectively

## RESISTANCE MEASUREMENT

Patterns to be printed were designed in a CAD modeling software. Figure 6 shows the design of the resistive pattern used for quantification of resistance as a function of process parameters. The pattern shown in Figure 6 with 4-units was printed on the substrates, for the previously selected process parameters of ink mass flow rate, sheath gas flow rate, stage speed, standoff height, nozzle diameter, and number of passes.

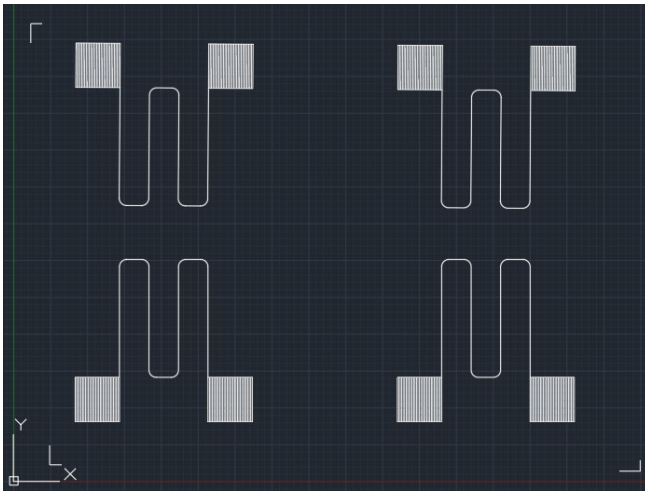


**Figure 6:** CAD of the pattern to be printed

In order to measure the resistance, aluminum based conductive epoxy mixed as per the stipulated ratio was deposited on the pads and a wire was connected using a conductivity epoxy mixed in the ratio of 1:2. The resistance was measured using a digital multimeter by probing the connected wires. An average of four resistance values obtained per print per condition has been reported for each reported resistance measurement in the paper.

### SHEAR LOAD TO FAILURE

Additive or subtractive 3D printed electronics may be subjected to shear and torsion loads during manufacturing, assembly or service. The print pattern shown in Figure 6 was printed and cured at the different sintering temperatures and times shown in Table 5 and Table 6. A Dage shear tester shown in Figure 7 was used to apply a shear load using a knife edge. The failure load reported, once the transverse cross-section failed was reported. An average of 6 values was reported for each condition measured in the study.

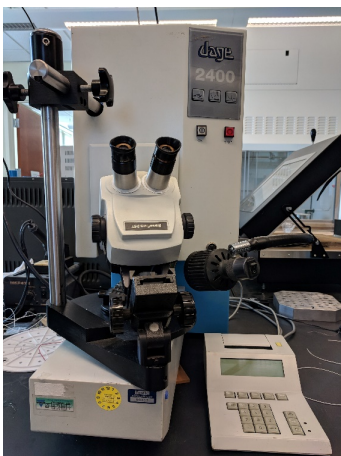


**Figure 7:** Dage Ball Shear Tester

### MEASUREMENT OF ELASTIC MODULUS

Elastic modulus of the silver lines printed lines was experimentally measured using a nano-indentation technique. This technique involves using a pointed indenter to indent the

surface of sample. The displacement of the indenter as a function of applied force is recorded as a function of time through the loading and the unloading cycle of the test. During the loading cycle, the indenter undergoes both elastic and plastic deformation. Several methods for computing the elastic modulus and hardness have been published. In this work, the Oliver-Pharr method has been used to compute the mechanical properties from the nano-indenter load displacement curves. The hardness,  $H$  is defined as the mean pressure under the indenter [Oliver 1992],

$$H = \frac{P_{\max}}{A_c} \quad (1)$$

Where,  $P_{\max}$  is the maximum applied force and is obtained from the load vs displacement graph,  $A_c$  is the projected area of the indenter tip. For a perfect Berkovitch indenter the contact area can also be represented as:

$$A_c = 24.56h_c^2 \quad (2)$$

Where,  $h_c$  is the contact depth of the indenter tip. The slope of the unloading curve can be used to compute the elastic modulus using  $E_r$ , the reduced modulus of the specimen. For a Berkovitch indenter, the contact stiffness is given as follows:

$$S = \frac{2}{\sqrt{\pi}} E_r \sqrt{A_c} = \frac{dP}{dh} \quad (3)$$

Where,  $S$  is the contact stiffness.  $P$  and  $h$  are the indenter force and indenter height. Equation (3) can be rearranged to obtain,

$$\frac{1}{E_r} = \left(\frac{\pi}{4}\right)^{1/2} \left(\frac{1}{A_c}\right)^{1/2} \quad (4)$$

The measured elastic modulus has contributions from both the specimen and the indenter which are related as follows,

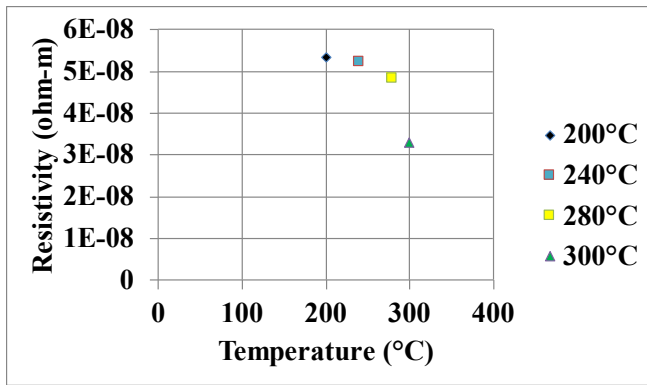
$$\frac{1}{E_r} = \frac{1 - \nu_s^2}{E_s} + \frac{1 - \nu_i^2}{E_i} \quad (5)$$

Where,  $\nu_s$  and  $\nu_i$  are the Poisson's ratio of the indenter and specimen. From equation above, the elastic modulus for thin films samples can be given as,

$$E_s = \left(\frac{1}{E_r} - \frac{1 - \nu_i^2}{E_i}\right)^{-1} \quad (6)$$

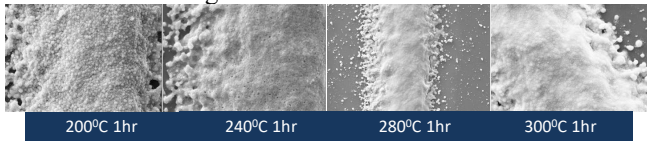
### EFFECT OF SINTERING TEMPERATURE ON RESISTIVITY

Figure 8 shows the graph of resistivity with respect to change in sintering temperature. The sintering time has been kept constant for all the measurements at 60-min of thermal sintering at specified temperature. Experimental measurements indicate that the resistivity decreases with the increase in sintering temperature.



**Figure 8:** Resistivity Vs Sintering Temperature for Conductive Ink-A

The resistivity decreases or improves with increasing sintering temperature. In order to understand the physics of changes in resistivity, scanning electron microscopy images were taken to investigate the resistivity measurements (Figure 9). A comparison of the images from 200°C @1-hr with the images for 300°C @1-hr reveals that the nanoparticle in the printed ink are more clearly visible at lower sintering times. Nanoparticles are not discernable in sintering conditions of 300°C @1-hr. Increase in sintering temperature allows the nanoparticles to coalesce more readily resulting in a reduction in the resistivity of the printed traces. The trend is consistent for sintering temperature of 240°C, and 280°C sintering for 1-hour.



**Figure 9:** SEM images for varying sintering temperature and constant sintering time for Conductive Ink-A

### EFFECT ON SINTERING TIME ON RESISTIVITY

The effect of sintering time has been measured by decoupling the effect of the sintering temperature in this part of the measurements. The sintering temperature has been kept constant at 200°C for the specified period of time. Figure 10 shows the graph of resistivity with respect to changes in sintering time. Experimental measurements indicate that the resistivity increases with increase in sintering time.

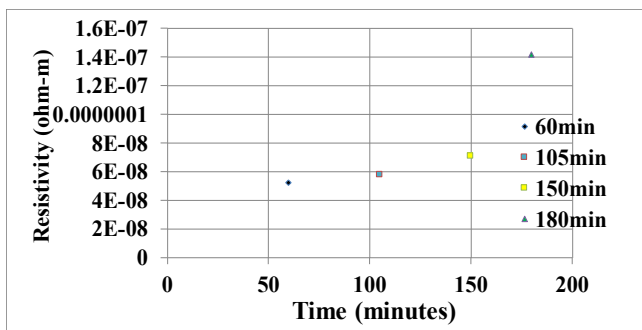


**Figure 10:** Resistivity Vs Sintering Time for Conductive Ink-A

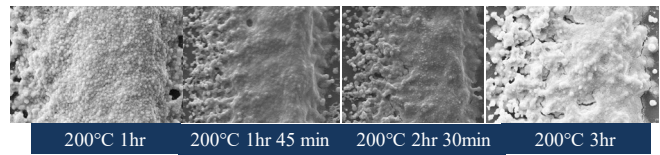


**Figure 11:** SEM imagery for varying sintering time for Conductive Ink-A

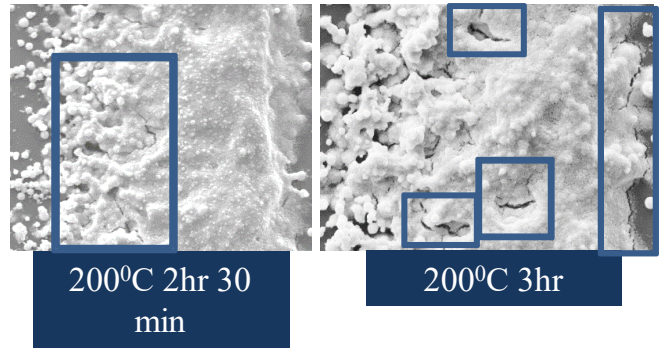


**Figure 12:** Appearance of micro-cracks for Conductive Ink-A

Resistivity increases or degrades with the increase in sintering time for a specified sintering temperature. In order to understand the physics of changes in resistivity, scanning electron microscopy images were taken to investigate the resistivity measurements (Figure 11). A comparison of the images from 200°C @1-hr with the images for 200°C @3-hr reveals that the nanoparticle in the printed ink are more clearly visible at lower sintering times. Nanoparticles are not discernable in sintering conditions of 200°C @3-hr. Increase in sintering temperature allows the nanoparticles to coalesce more readily resulting in a reduction in the resistivity of the printed traces.

Higher sintering conditions also show appearance of micro cracks in the printed lines after sintering. The locations of microcracks are highlighted with blue-rectangles in Figure 12. The elimination of point-contact between particles results in a lower resistivity with the increase in sintering time. The trend is consistent for sintering temperature of 240°C, and 280°C sintering for 1-hour. The opposite trend of the increase in resistivity with the increase in sintering time is due to the appearance of micro cracks, which increase the current density in the printed-trace due to reduction in effective cross-sectional area. The occurrence of micro-cracks could be attributed to the evaporation of solvent and co-solvent that are deposited on the substrate prior to sintering. Ethylene glycol is the solvent in this ink, mixed with water and other co-solvents. The boiling point of the ethylene glycol as published in data sheets is 197.1°C. This residual chemical may undergo boiling when sintered for longer duration and escape out of the lines leaving cracks. A higher mean free path of electrons corresponds to higher resistivity because more scattering is observed as higher resistance. The presence of cracks would increase the mean free path of the electrons, increasing the resistance and in turn

deteriorate the resistivity. Figure 9 show the scanning electron microscopy images for lines sintered for 1 hour and for increase in the sintering temperature.

### EFFECT OF SINTERING TEMPERATURE ON THE SHEAR LOAD-TO-FAILURE

A Dage shear tester with a knife-edge was used to find the shear load to failure for lines printed at varying sintering temperatures at a sintering time of 1-hr. Figure 13 shows the graph of shear load to failure with increase in sintering temperature.

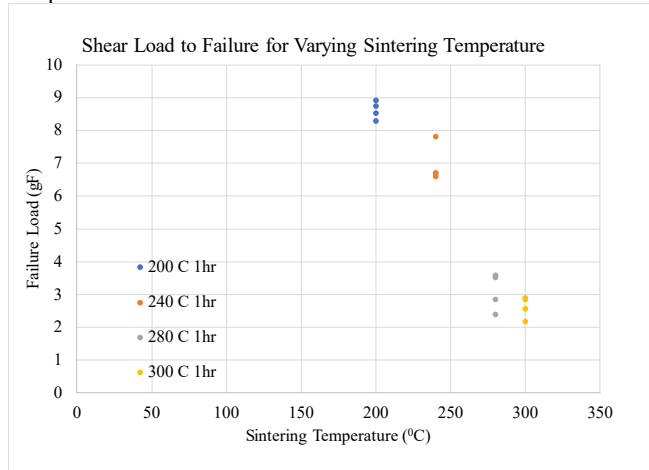


**Figure 13:** Shear Load to Failure Vs Sintering Temperature for Conductive Ink-A

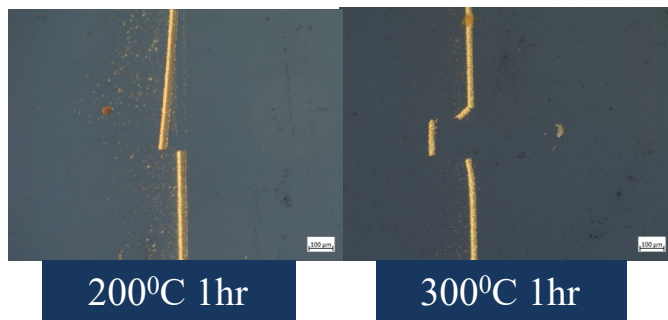


**Figure 14:** Sheared line for increasing sintering temperature for Conductive Ink-A

Experimental data indicates that the shear load-at-failure reduces with the increase in sintering temperature. The optical images of the sheared lines for increasing sintering temperature are shown in Figure 14. Sintering process is known to result in increase in nano-particle volume fraction, caused due to solvent evaporation. The sheared line for 200°C, 1-hour sintering condition shows a relatively ductile failure in comparison to the sheared line for 300°C, 1-hour sintering condition. When the printed line may be sintered for a prolonged period, the silver nano-particles coalesce resulting in making the structure more brittle, and a reduction in the ultimate tensile strength. This explains the transition from a ductile to brittle behavior of the printed lines shown in Figure 14.

### EFFECT OF SINTERING TIME ON THE SHEAR LOAD-TO-FAILURE

A Dage shear tester with a knife-edge was used to find the shear load to failure for lines printed at varying sintering time at a sintering temperature of 200°C. Figure 15 shows the graph of shear load to failure with increase in sintering time. Experimental data indicates that the shear load-at-failure reduces with the increase in sintering time. The optical images of the sheared lines for increasing sintering time are shown in Figure 16.

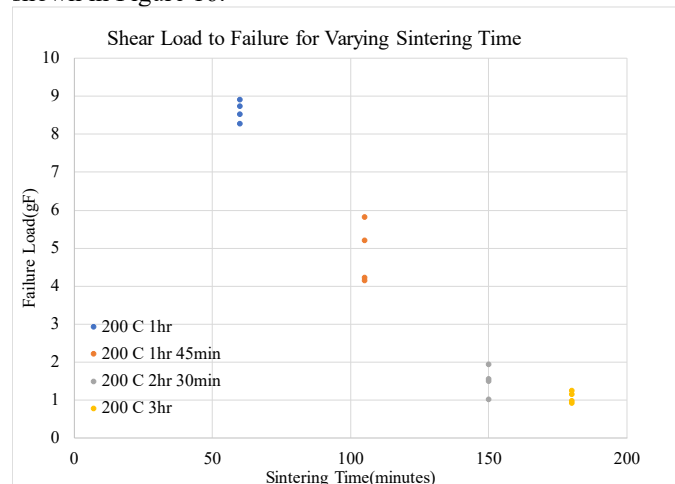


**Figure 15:** Shear Load to Failure Vs Sintering Time for Conductive Ink-A

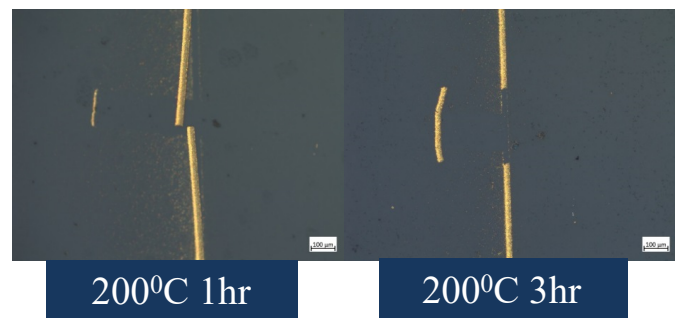


**Figure 16:** Sheared line for increasing sintering time for Conductive Ink-A

Sintering process is known to result in increase in nano-particle volume fraction, caused due to solvent evaporation. The sheared line for 200°C, 1-hour sintering condition shows a relatively ductile failure in comparison to the sheared line for 200°C, 3-hour sintering condition. When the printed line may be sintered for a prolonged period, the silver nano-particles coalesce resulting in making the structure more brittle, and a reduction in the ultimate tensile strength. This explains the transition from a ductile to brittle behavior of the printed lines shown in Figure 16.

### EFFECT OF SINTERING TEMPERATURE ON ELASTIC MODULUS

Aerosol jet printed samples were printed, potted in resin and polished for the nano-indentation tests. A load of 20,000 micro-newtons was applied to the samples that resulted in an indentation depth of 920nm. A relatively high load was used to measure elastic modulus in the bulk region and avoid the influence of surface roughness. Figure 17 shows the effect of varying sintering temperature on elastic modulus. Elastic modulus was found to decrease monotonically with the increase in sintering temperature from 200°C to 300°C for a sintering time of 1-hour.

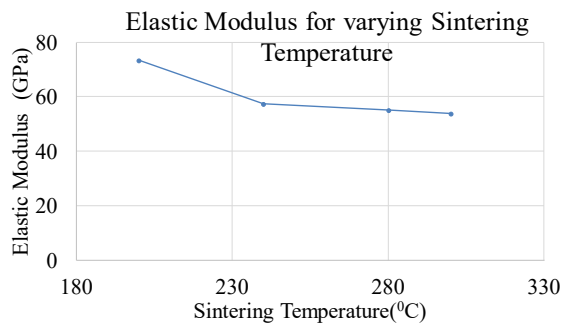


**Figure 17:** Elastic modulus for varying sintering temperature for Conductive Ink-A

A 26-percent reduction in elastic modulus was found between the printed lines sintered at 300°C for 1-hr with respect to the printed lines sintered at 200°C for 1-hr. This reduction may be attributed to the degradation of grain boundaries at a higher temperatures.

### LONG TERM LINE PRINT CONSISTENCY

In order to investigate the long-term print consistency of the conductive line using the AJP process, conductive ink-A was used with the an ultrasonic atomizer. For longer print durations, a bubbler for solvent replenishing was also used to maintain the viscosity of the ink. The results in this section are presented with and without the presence of bubbler.

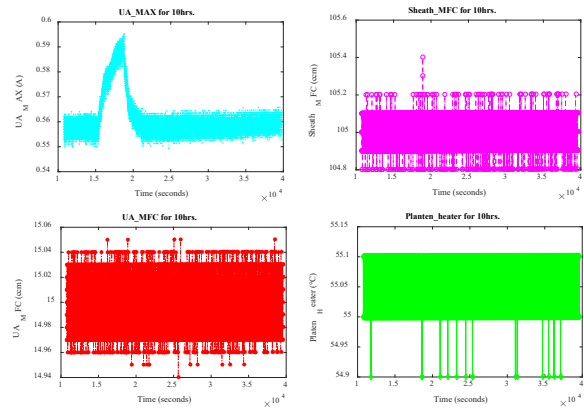


**Figure 18:** Variation in process parameters with bubbler for Conductive Ink-A

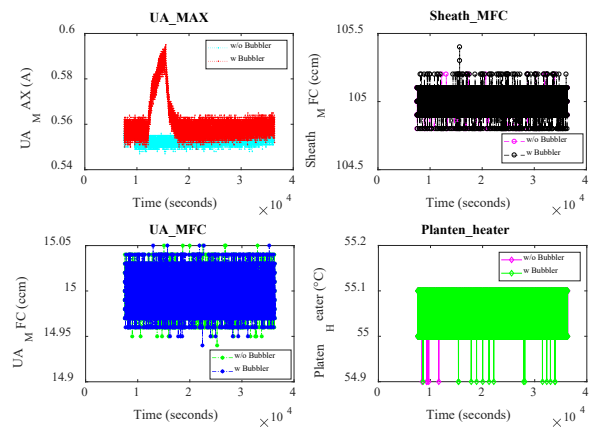


**Figure 19:** Comparison of the Process Parameters with and without Bubbler for Conductive Ink-A

**Table 7:** Response values of the Process Parameters for Conductive Ink-A

Parameter	Control Values	Mean	STD Dev	Variance
ShFR	105	104.99	0.0564	0.0032
CFR	15	14.99	0.0127	1.62e-4
UA_MAX (mAmps)	0.56	0.561	0.0081	6.52e-5
Platen Heater (°C)	55	55.003	0.0178	3.18e-4

The drift in the process parameters was quantified and their effect on the dimensions of the printed lines studied. For the purpose of this study, the Aerosol jet printer was allowed to print continuously for a duration of 10 hours using the ultrasonic atomizer. Printing process consistency was gauged through the quantification of process capability index ( $C_{pk}$ ) and process capability ratio ( $C_p$ ).

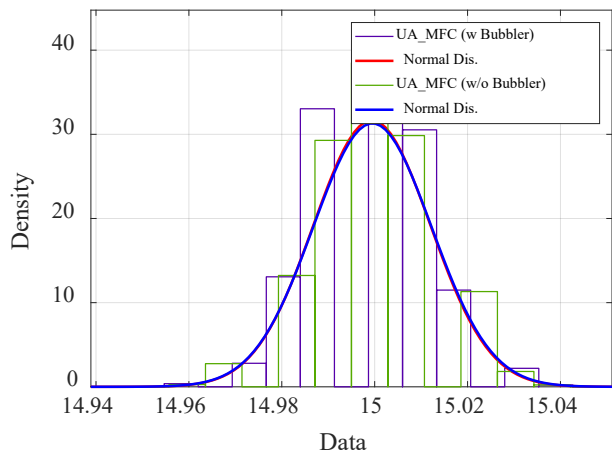


**Figure 20:** Probability Density Function of CFR fitted with Normal Distribution for Conductive Ink-A

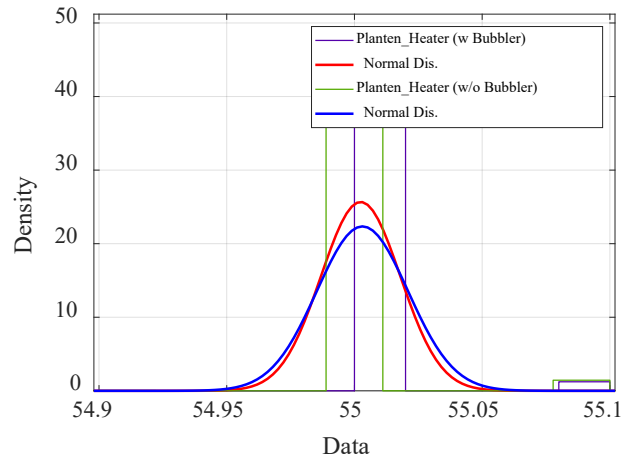


**Figure 23:** Probability Density Function of Platen Heater fitted with Normal Distribution for Conductive Ink-A

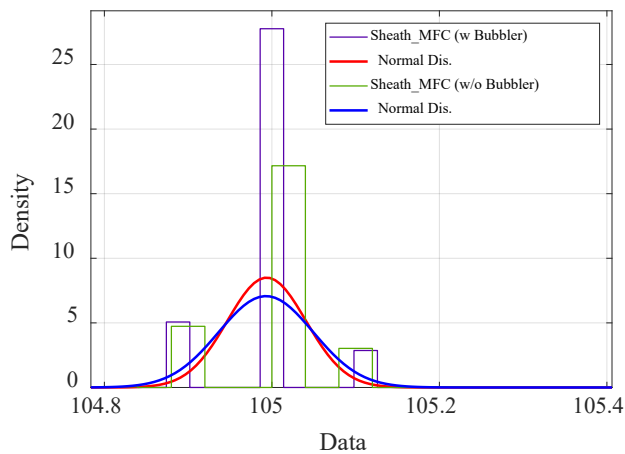


**Figure 21:** Probability Density Function of ShFR fitted with Normal Distribution for Conductive Ink-A

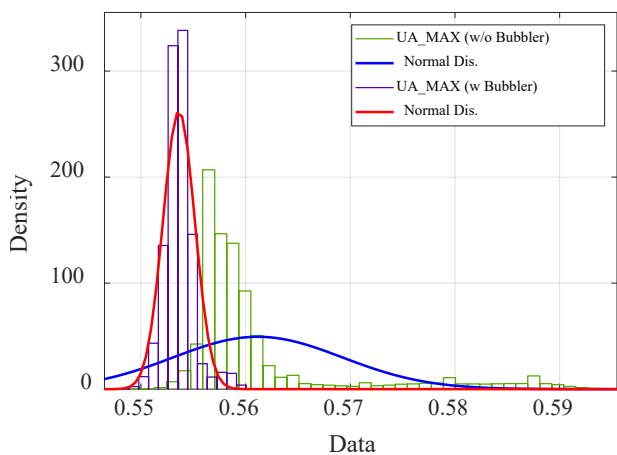


**Figure 22:** Probability Density Function of UA\_MAX fitted with Normal Distribution

Four main parameters, nitrogen or sheath gas flow rate (ShFR), carrier gas flow rate (CFR), ultrasonic atomizer current (UA\_MAX) and platen heater, which influence the print quality, were recorded in-situ for the entirety of the tests conducted. Figure 18 shows the four process parameters recorded for a period of 10 hours. The control values were pre-defined before start of the 10-hour cycle count; these values are listed in Table 7. It can be seen from Table 7 how the response values correspond with the control values. Probability density functions (PDFs) of the process parameters fitted with normal distributions are shown in Figure 20 through Figure 23 to assess the likelihood that the random values of the process parameters will be close to the actual set-value of the parameter. The data is shown with and without the use of bubbler. The variance in the CFR, ShFR, UA\_MAX, Platen Heater Temperature, is lower with the use of a bubbler in all cases. The PDFs were computed for the full 10 hour using in-situ data.

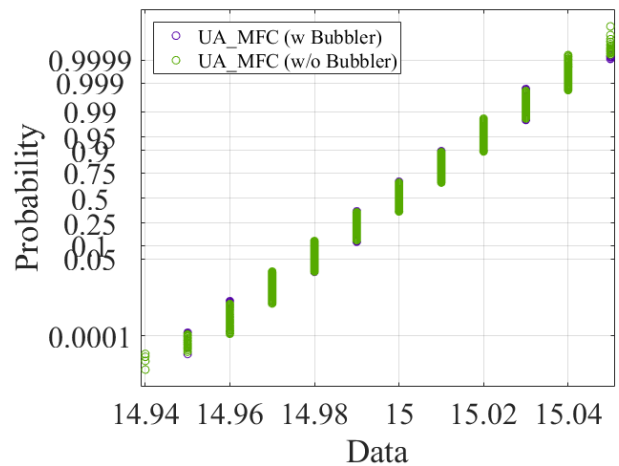


**Figure 24:** Accumulated Probability plot for CFR for a 10 hour run for Conductive Ink-A

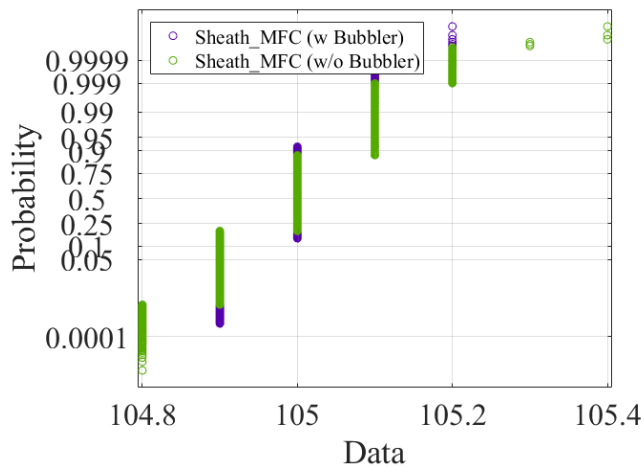


**Figure 25:** Accumulated Probability plot for ShFR for a 10 hour run for Conductive Ink-A

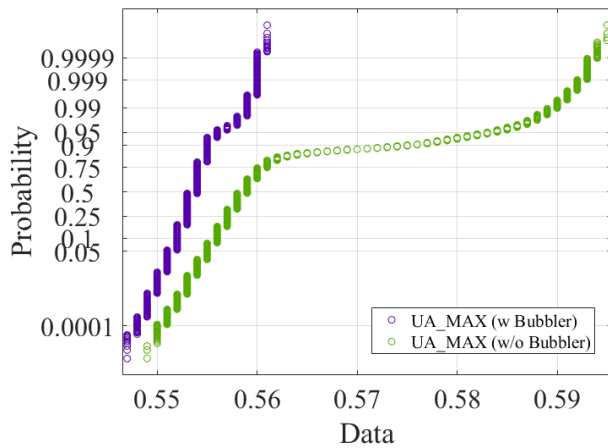


**Figure 26:** Accumulated Probability plot for UA\_MAX for a 10 hour run for Conductive Ink-A

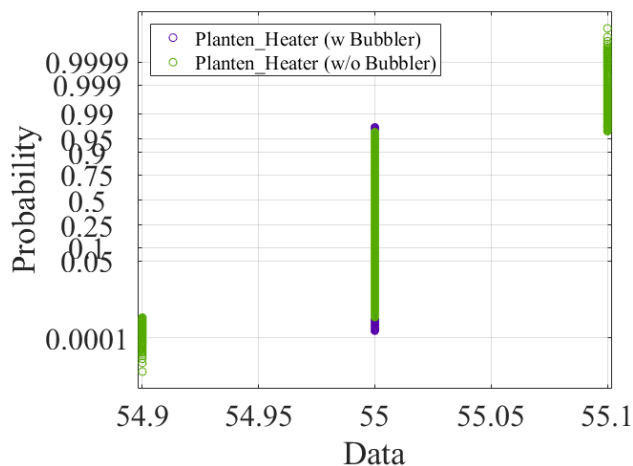


**Figure 27:** Accumulated Probability plot for Platen Heater for a 10 hour run for Conductive Ink-A

Figure 24 thru Figure 27 show the probability plots for the four process parameters where the distribution of the data in x is compared to the normal distribution. The data is plot against a theoretical normal distribution. For a normal distribution, the points should form an approximate straight line and any deviation from the straight line indicates deviations from normality. An example can be seen in Figure 26, which shows the probability plot for UA\_MAX. The curvature can be attributed to the spike observed in the atomizer current data shown in top left of Figure 18.

### DIMENSIONAL PARAMETERS

The printed dimension of the lines was used to compute the effect of print run on the dimensional consistency of the printed traces. Print line width and line height were computed by conducting surface-profilometry experiments whereas the pattern resistance was computed using a 4-point resistance method using a resistance probe.

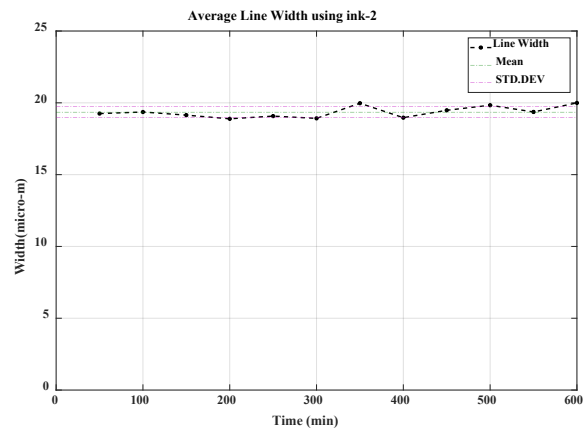


**Figure 28:** Average Line Width of the printed samples with Bubbler for Conductive Ink-A

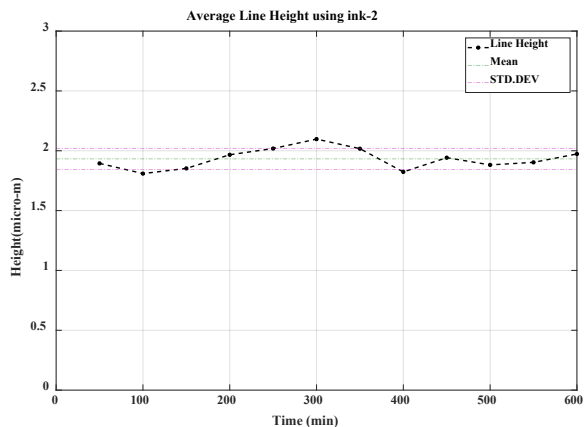


**Figure 29:** Average Line Width of the printed samples with Bubbler for Conductive Ink-A

Figure 28 and Figure 29 show that the average line width was between 19-20 $\mu$ m whereas the average line height was between 1.8-2 $\mu$ m. Over the course of the 10-hr print-period, the line dimensions show variations mainly along the height of the printed line. These variations do increase and decrease with time and the line height does not stay constant whereas

the variations along the line width seem to be constant during first 300 minutes of printing but then drift positively or negatively as the print time increases.

### PRINT RESISTANCE VS RUN TIME

Several substrates were printed over the 10-hour period, where each print-run represents 50-min of print time. The printed pattern has been described about in the above sections. Each sample (glass slide) has 4-patterns, below shown is the print resistance as a function of operational time in Figure 30. Each data point on the resistance plots is an average of the 4-patterns (for each slide representing their respective time instances).

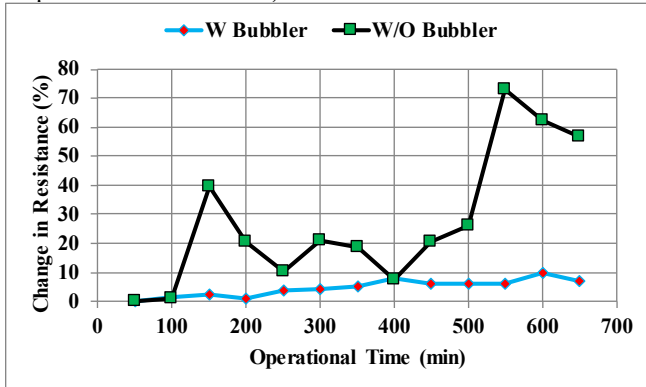


Figure 30: Print Resistance with and without bubbler for Conductive Ink-A

### LINE PRINT QUALITY VS PRINT-TIME

Optical images were used to visualize any evidence of variation in the print quality as a function of print-time. It was also observed from the dimensional plots (Figure 28 and Figure 29) that line width tends to remain within  $\pm\sigma$  (one standard deviation mark) whereas the line height shows variance, which violates the one standard deviation limit.

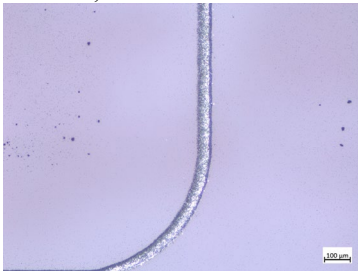


Figure 31: Print Quality of the loop feature from the pattern at 50<sup>th</sup> min mark for Conductive Ink-A

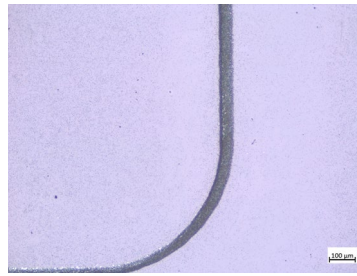


Figure 32: Print Quality of the loop feature from the pattern after 10th hour mark for Conductive Ink-A

Figure 31 and Figure 32 show a comparison of the print quality at the 50-min mark with that of the 10-hour print run mark. The prints appear comparable with the use of a bubbler and no significant change in the quality of the printed line is observed.

### CONDUCTIVE INK-B w/ULTRASONIC ATOMIZER

A study was done to predict the line width and the resistance. Main effects and only two-way interactions are considered. Since this is a low viscosity metal ink, it is easier to have more controllable factors as compared to in the case of dielectric. Table 8-Table 10 list the controlled factors, constant factors, and the output responses.

Table 8: List of Varied Factors

Varied Factors				
UA_MFC (sccm)	Sheath (sccm)	Print Speed (mm/s)	Standoff Height (mm)	Number of Passes
4	3	3	3	3
Levels	Levels	Levels	Levels	Levels
{10}	{50}	{3}	{2}	{3}
{15}	{100}	{5}	{3}	{5}
{20}	{150}	{7}	{4}	{10}
{25}				

Table 9: List of Constant Factors

Constant Factors	
Platen Temperature (°C)	55
Chiller Temperature (°C)	14
Atomization	Ultrasonic
Conductive Ink Material	Ag Nano-particle
Substrate	Glass
Substrate Pre-cleaning	5min IPA submerged and Ultrasonic cleaned with DI
Sintering	Layer 1: 100°C for 30 mins Layer 3: 300°C for 30 mins

**Table 10: Output Responses**

Output Responses	Line Width

**Figure 33:** Test design for the statistical model for conductive line width and resistance prediction

Using the information above, DOE matrix is created for the combination of test parameters. . Figure 33 shows the design for metal conductive lines consisting of multiple columns representing different combination of tests and five rows at the same test for repeatability. With the design provided in Figure 33, the study was carried out. The results are valid for Ink 1 with UA – however, the trends exhibited in various variables are more general to other materials as well. Figure 34 shows the list of 35 tests performed using UA for the conductive ink-B. For all of the tests, line widths predicted are within 15% of the actual line width measured optically. Results indicate a good correlation between the printed and expected line width.

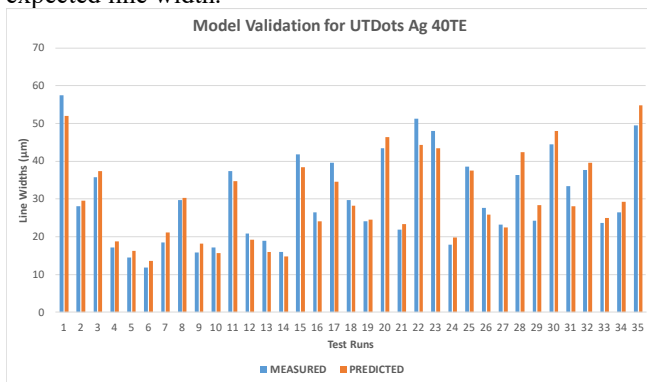


**Figure 34:** Results of 35 tests for Conductive Ink-B

**ILD INK-C USING PNEUMATIC ATOMIZER**

To perform the study, a list of varied and constant factors is made in addition to the output response. Table 11 provides the list of varied factors with their levels considered, while Table 12 provides the constant or fixed factors. Table 13 lists the output response. Figure 35 shows the design for the dielectric-via, which consists of multiple columns of via diameters representing different combination of tests and ten rows of the diameters at the same tests to check for repeatability

**Table 11:** List of Varied Factors for ILD Ink-C

Varied Factors			
PA_MFC (sccm)	Sheath (sccm)	Δ (PA_MFC – Exhaust) (sccm)	Print Speed (mm/s)
3 Levels { 1150 1200 1250 }	3 Levels { 50 75 100 }	3 Levels { 40 50 60 }	3 Levels { 0.3 0.5 0.6 }

**Table 12:** List of Constant Factors for ILD Ink-C

Constant Factors	
Platen Temperature (°C)	Room temperature
Atomization	Pneumatic
Dielectric Material	Adhesive
Substrate	Glass
Number of Passes	2
Nozzle (µm)	200
Substrate Pre-cleaning	5min IPA submerged and Ultrasonic cleaned with DI
Curing	UV Cure on the Fly

**Table 13:** Output Response

Output Response	Via Diameter

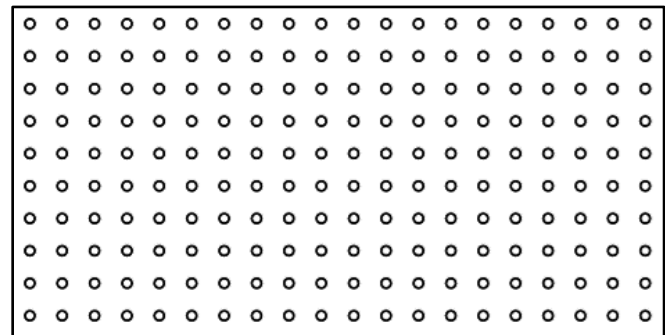


**Figure 35:** Test design for the statistical model for dielectric via diameter prediction

Using the information from above, DOE (Design-of-Experiment) matrix is created which provides us the combinations to perform the experiments on. With that matrix, and design discussed previously, the study is carried out. Ten rows of via diameters are printed at the same test condition, after which parameters are changed and so on. Note that this is valid for only Ink 2 with PA. In addition, the range of the controlled factors are chosen to be very close to each other to get a connected line for the diameter measurement. Increasing the range gives us unconnected line at some levels, which can produce errors in the model.

**EFFECT OF UV INTENSITY AND SINTERING ON MICRO-VIA**

This section discusses the effect of different UV intensities and uneven sintering conditions for Layer 1 and Layer 3 used to cure ILD Ink-C and the Ag metal conductive line with Ink-B respectively. The UV system used is from Panasonic, model Aicure UJ35. It consists of four individually controlled UV-LED heads with cylindrical lenses to spot cure. Fixtures are designed to hold the LED in place on the AJP machine to UV cure while the toolpath is running. From Figure 36, a clear distinction can be seen when Ink-C is cured at two different intensities i.e. 50% and 100%. Similarly, curing the metal line with proper set of temperatures is just as important for multi-layer structures in which layer-1 is metal, layer-2 is ILD and layer-3 is metal with z-axis interconnects.



**Figure 36:** Effect of UV Intensity on the Via for ILD Ink-C

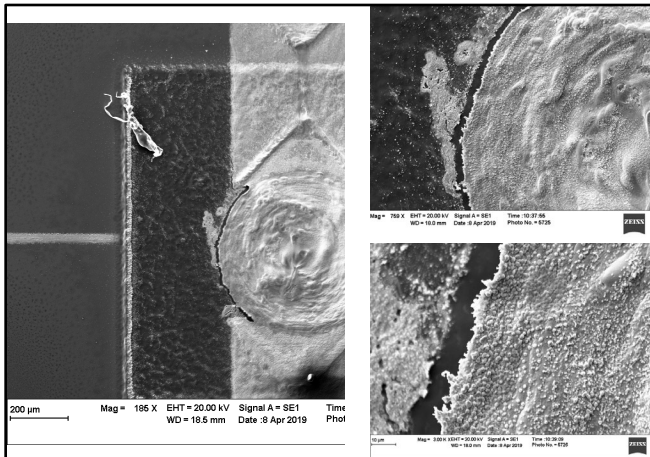


**Figure 37:** Effect of over-sintering the Via (200°C/60mins for Layer 1; 300°C/60mins)

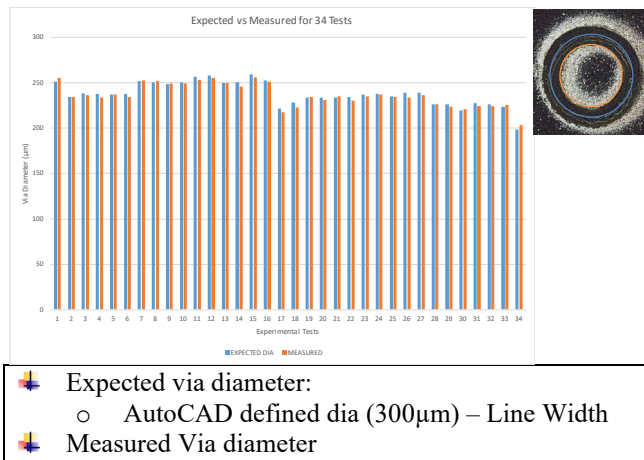


**Figure 38:** Via Diameter measurements for the 34 Tests performed

Layer 1, which is sintered at specific temperature previously, will be exposed to another sintering condition when Layer 3 is getting cured. Figure 37 shows an interface crack between Ag and dielectric when the curing conditions were 200°C/60 min for Layer 1 and 300°C/60 min. The best combination of sintering parameters were determined by varying the

temperature and time, and measuring their effect on the line resistance and shear load to failure. Using the results, Layer 1 was sintered at 100°C/30mins and Layer 2 at 300°C/30mins. From the modeled DOE, 34 combination of tests were performed using the dielectric ink and the via diameter was measured for all of them. Figure 38 below shows a comparison graph for the via diameter expected vs. measured for those tests. The expected diameter is the one modeled through AutoCAD. The measured diameters were recorded as the response to input into the statistical model. Results indicate good convergence between the predicted and measured diameters of the vias.

### MULTI-LAYER STRUCTURE w/Z-INTERCONNECT

The optimized process parameters were used to fabricate a multi-layer structure with z-axis interconnects. Process study consists of creating a micro-via with “optimum” set of AJP parameters, curing conditions, and most importantly, pre-cleaning of the substrate. Figure 39 below shows a complete micro-via with the AJP parameters listed in Table 14-Table 15.

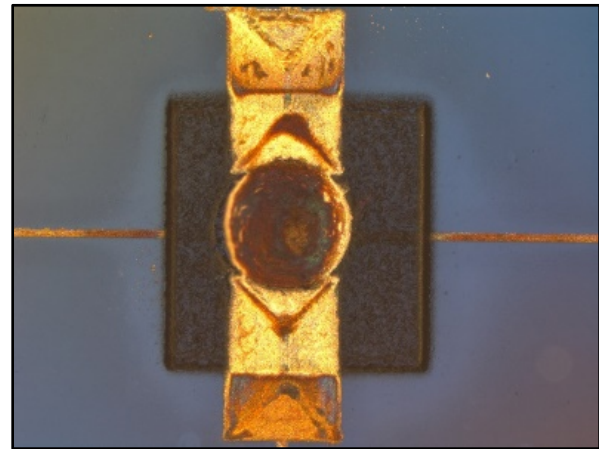


**Figure 39:** Micro-Via

**Table 14:** Set of Process Parameters for the Micro-Via

Process Parameters for Dielectric	
Carrier Flow Rate (sccm)	1200
Sheath (sccm)	50
Exhaust or Δ (sccm)	1150 or 50
Print Speed (mm/s)	0.5
Standoff Height (mm)	2
Nozzle (μm)	200
Number of Passes	2
Curing	UV Cure on the Fly
Pre-Cleaning	5min IPA submerged and Ultrasonic cleaned with DI

**Table 15:** Set of Process Parameters for the Metal Ink

Process Parameters for Ag Nanoparticle Ink	
Carrier Flow Rate (sccm)	18
Ultrasonic Current (A)	0.54 – 0.56
Sheath (sccm)	100
Print Speed (mm/s)	5
Standoff Height (mm)	2
Nozzle (µm)	200
Number of Passes	5
Sintering	Layer 1: 100°C for 30 min Layer 3: 300°C for 30 min
Pre-Cleaning	5min IPA submerged and Ultrasonic cleaned with DI water

**STATISTICAL ASSESSMENT OF PROCESS**

The 10-hour long print consistency was studied using a statistical approach to quantify process robustness. In this work, we showcase the potential of the four control variables including. ShFR, CFR, UA\_MAX and Platen Heater and three response variables line-width, line-thickness, and line resistivity as a function of process capability index (C<sub>pk</sub>) and process capability ratio (C<sub>p</sub>). Two questions, which are answered using this approach, are - (a) How does one statistically characterize the printing process? (b) Is this process under control for reliable use?

$$C_p = \frac{(\text{UpperSpecLimit}) - (\text{LowerSpecLimit})}{6\sigma} \quad (7)$$

$$C_{pk1} = \frac{(\text{UpperSpecLimit}) - (X_{50})}{3\sigma} \quad (8)$$

$$C_{pk2} = \frac{(X_{50}) - (\text{LowerSpecLimit})}{3\sigma} \quad (9)$$

Where X<sub>50</sub> is the mean value of the variable, and σ is the standard deviation. The equations listed above represent the process capability indexes (C<sub>pk</sub>) and process capability ratio (C<sub>p</sub>). The tolerances for the four process parameters were established using measurement of variance from the respective mean values.

**Table 16:** Process Capability of control and print parameters WITHOUT Bubbler FOR Conductive Ink-A

	Platen	Sheath	UA	UA_Max	Resistance
C <sub>p</sub>	1.0727	1.0656	1.0583	1.0963	0.767
C <sub>pk1</sub>	1	1.01	1.011	1.096	0.744
C <sub>pk2</sub>	1.01	1	1.01	1.1	0.732

**Table 17:** Process Capability of control and print parameters WITH Bubbler

	Platen	Sheath	UA	UA_Max	Resistance	Height	Width
C <sub>p</sub>	1.067	1.043	1.051	1.089	1.224	1.09	1.06
C <sub>pk1</sub>	1.001	1	1.031	1.002	1.226	1.02	1.03
C <sub>pk2</sub>	1.01	1.022	1	1	1.213	1	1.01

The main task of this approach is to find whether or not we can fit six standard deviations within this range to form a basis of a 6σ capable process. Three-sigma processes have a C<sub>pk</sub> of 1 and six-sigma processes have a C<sub>pk</sub> of 2. Process capability ratio and indexes have been established for CFR (UA\_MFC). Table 16 and Table 17 show the computation for the process capability index (C<sub>pk</sub>) and process capability ratio (C<sub>p</sub>) for configuration with the bubbler and without the bubbler respectively. The via-printing process exhibits a Cp of 1.1 and Cpk of 0.65 (Figure 40).

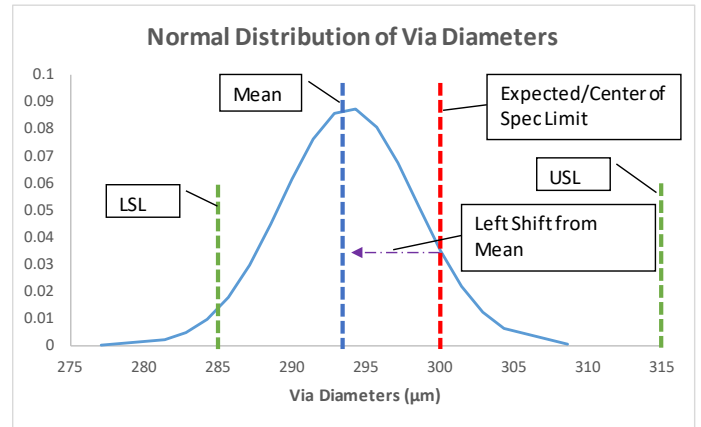


**Figure 40:** Distribution of Via Diameters

$$C_p = \frac{315 - 285}{6(4.54)} = 1.10$$

$$C_{pk} = \min\left(\frac{315 - 294}{3(4.54)}, \frac{294 - 285}{3(4.54)}\right) = 0.65$$

The values of the process capability index (C<sub>pk</sub>) and process capability ratio (C<sub>p</sub>) have been computed for both the control parameters and the print-performance parameters. A process capability of 1 indicates a 3-sigma process and a process capability of 2 indicates a 6-sigma process. Computations in Table 16 indicate that without bubbler, the resistance consistency is approximately a 2.125-sigma process. Computations in Table 17 indicate that with bubbler, the resistance consistency is approximately a 3.6-sigma process, height consistency is approximately 3-to-3.25-sigma process, and width consistency is a 3-to-3.25-sigma process.

**SUMMARY AND CONCLUSIONS**

In this paper, a detailed study of the effect of aerosol-jet process parameters on the resistance, shear strength, and elastic modulus has been presented. Experimental

measurements indicate that the resistivity improved with the increase in the number of passes. Increase in sintering time at a constant sintering temperature was found to increase resistivity of the printed line resulting from the increase in number of cracks in the printed lines. Multi-layer print process is developed and different parameters that adversely affect the print quality are studied. Parameters such as UV Curing for the dielectric, and sintering temperature for the metal ink, are found to be of great influence to the print quality of the micro-via. Increase in the sintering temperature at a constant sintering time was found to decrease the resistivity of the printed line – which based on SEM analysis can be attributed to the decrease porosity of the printed line. Mechanical properties including the elastic modulus and shear strength decreased with the increase in sintering temperature. Line-consistency measurements of line-width, line height, and resistance over a continuous 10-hour print run are reported. Process measurements indicate that viscosity of the ink has a pivotal role in maintaining print consistency. Line width, line height, and resistance measurements exhibit much lower variance with the use of bubbler, which enables control over ink-viscosity during the 10-hour print run. In addition, computation of the process capability index ( $C_{pk}$ ) and process capability ratio ( $C_p$ ) indicate that without bubbler, the resistance consistency is a 2.125-sigma process. Further, the use of bubbler allows for a wider process window where, resistance consistency is a 3.6-sigma process, height consistency is 3-to-3.25-sigma process, and width consistency is a 3-to-3.25-sigma process. The via-printing process exhibited a  $C_p$  of 1.1 and  $C_{pk}$  of 0.65.

#### ACKNOWLEDGEMENTS

The project was sponsored by the NextFlex Manufacturing Institute under OPC 1.0 Open Call Project titled – Additive and Semi-Additive Methods for High-Density Interconnects. This material is based, in part, on research sponsored by Air Force Research Laboratory under agreement number FA8650-15-2-5401, as conducted through the flexible hybrid electronics manufacturing innovation institute, NextFlex. The U.S. Government is authorized to reproduce and distribute reprints for Governmental purposes notwithstanding any copyright notation thereon. The views and conclusions contained herein are those of the authors and should not be interpreted as necessarily representing the official policies or endorsements, either expressed or implied, of Air Force Research Laboratory or the U.S. Government.

#### REFERENCES

- [1] BCC Research, Printed Electronics: The Global Market, <https://www.bccresearch.com/market-research/information-technology/printed-electronics-market-ift066b.html>, 2012
- [2] Binder S, GlatthaarMand Rädlein E 2014 Aerosol Sci. Technol. 48 924
- [3] Cai, F., Aerosol jet printing for 3-D multilayer passive microwave circuitry, 44th European Microwave Conference, pp. 512-515, 2014.
- [4] Ha M, Zhang W, Braga D, Renn, MJ, Kim, CH and Frisbie CD 2013 ACS Appl. Mater. Interfaces 5 13198

- [5] IDTECHX 2018: <https://www.idtechx.com/research/articles/printed-electronics-key-trends-00015712.asp>, Raghu Das, October 2018
- [6] Khorramdel, B., A. Torkkeli and M. Mäntysalo, Electrical Contacts in SOI MEMS Using Aerosol Jet Printing, in IEEE Journal of the Electron Devices Society, vol. 6, pp. 34-40, 2018.
- [7] King, B. H., M. J. O'Reilly and S. M. Barnes, "Characterizing aerosol Jet@multi-nozzle process parameters for non-contact front side metallization of silicon solar cells," 34th IEEE Photovoltaic Specialists Conference (PVSC), Philadelphia, PA, pp. 001107-001111, 2009.
- [8] Krzeminski, J., Pads and microscale vias with aerosol jet printing technique, 2017 21st European Microelectronics and Packaging Conference (EMPC) & Exhibition, Warsaw, pp. 1-4, 2017
- [9] Lang R J 1962 J. Acoust. Soc. Am. 34 6
- [10] Lupo, D., W. Clemens, S. Breitung, K. Hecker, E. Cantatore, "Oe-a roadmap for organic and printed electronics" in Applications of Organic and Printed Electronics, US:Springer, pp. 1-26, 2013.
- [11] Markets and Markets, Printed Electronics: <https://www.marketsandmarkets.com/PressReleases/printed-electronics-market.asp>, accessed, Dec 2018.
- [12] Navratil, J., T. Rericha, R. Soukup and A. Hamacek, "Aerosol Jet Printed Sensor on Fibre for Smart and IoT Applications," 2018 41st International Spring Seminar on Electronics Technology (ISSE), Zlatibor, pp. 1-4, 2018.
- [13] Oakley, C., A. Kaur, J. A. Byford and P. Chahal, Aerosol-Jet Printed Quasi-Optical Terahertz Filters, 67th ECTC, pp. 248-253, 2017.
- [14] Oliver, W. C., G. M. Pharr, An improved technique for determining hardness and elastic modulus using load and displacement sensing indentation experiments, J. Mater. Res., vol. 7, no. 6, pp. 1564-1583, June 1992.
- [15] Paulsen, J. A., M. Renn, K. Christenson and R. Plourde, "Printing conformal electronics on 3D structures with Aerosol Jet technology," Future of Instrumentation International Workshop (FIIW) Proceedings, Gatlinburg, TN, pp. 1-4, 2012.
- [16] Peskin R L and Raco R J, J. Acoust. Soc. Am. 35 1378, 1963
- [17] Ravindran P and Davis E J, J. Colloid Interface Sci. 85 278, 1982
- [18] Rodes C, Smith T, Crouse R and Ramachandran G, Aerosol Sci. Technol. 13 220, 1990
- [19] Secor, E., Principles of Aerosol Jet Printing, Flexible and Printed Electronics, 035002, 2018.
- [20] Stoukatch et al., Evaluation of Aerosol Jet Printing (AJP) technology for electronic packaging and interconnect technique, 4th Electronic System-Integration Technology Conference, Amsterdam, Netherlands, pp. 1-5, 2012.
- [21] Widmann J F and Davis E J, Aerosol Sci. Technol. 27 243, 1997